



An *in silico* analysis of unsteady flow structures in a microaxial blood pump under a pulsating rotation speed

Chenghan Chen^{a,b}, Mingkui Zhang^b, Pengfei Hao^a, Feng He^a, Xiwen Zhang^{a,*}

^a Applied Mechanics Laboratory, Department of Engineering Mechanics, School of Aerospace Engineering, Tsinghua University, Beijing, PR China

^b Department of Cardiovascular Surgery, First Hospital of Tsinghua University, Beijing, PR China



ARTICLE INFO

Keywords:

Blood pump
Hemolysis
Heart modeling and simulation
Pulsating flow
Computational fluid dynamics

ABSTRACT

Background and objective: Ventricular assist devices (VADs) are generally designed to perform continuous flow. However, it has been proven that continuous flow, which is not a physiological hemodynamic state, may cause severe complications such as gastrointestinal bleeding, pulmonary hypertension, and ventricular suction. For these reasons, many pulsating blood pump control strategies have been proposed and have the potential for application in percutaneous ventricular assist devices (pVADs) or microaxial blood pumps. A few cases report extra hemolysis when introducing pulsating speed, while none involve blood pumps. This research's primary purpose is to evaluate the potential hemolysis of pVAD under pulsating flow conditions.

Methods: First, the pulsating flow state is deduced using a heart failure model and varying speed. The heart model is established according to the pathology state collected from a clinical check. The rotation speed and boundary physical state are set to fit the heart failure model. The computational fluid dynamics (CFD) method with the hemolysis prediction model is performed. Furthermore, we used proper orthogonal decomposition (POD) analysis to reconstruct the flow field and obtain more details about shearing and transporting effects.

Results: (1) As a variable rotational speed was introduced, no significant gain in hemolysis accumulation appeared in pVAD. This is quite different from long-term implantable VADs. (2) Pulsation affects hemolysis mainly through pressure (or normal stress). Variable rotational speed affects hemolysis mainly through flow instability. (3) Variable rotational speed will increase the instability and influence hemolysis by transporting and shearing effects, while the transporting effect is more significant.

Conclusions: The unsteady flow state will affect the spatial distribution of hemolysis, which should be taken into account during control strategy and impeller shape design.

1. Introduction

Cardiogenic shock (CS) is a severe complication that involves insufficient cardiac output and end-organ perfusion [1]. According to the Nationwide Inpatient Sample (NIS) in the United States, the patient number has doubled over a decade [2], while in China, nearly 2/3 of CS patients cannot receive cardiac perfusion therapy in time [3]. As an effective clinical supplement used in left ventricular (LV) unloading, Impella is a percutaneous implantable microaxial blood pump that has received widespread attention in clinical treatment and VADs development. It has been proven that Impella 5.0, for example, has a better effect than IABP in improving the hemodynamics of CS patients [4–6]. For those who need ECMO therapy, cases had a better prognosis when Impella CP was combined because it can ease the burden in LV caused by

ECMO [7]. Other types of blood pumps can also be considered during clinical treatment, such as Tandem Heart, Arotix, and MIRVAD [8,9]. Recently, a case has reported using multiple microaxial pumps in the aorta to produce more flow than only a single facility across the valve [10].

However, such microaxial blood pumps are always set to be continuous-flow or constant rotation speed (CRS), which may cause ventricular arrhythmias and other complications, especially when longer-term therapy is considered [11,12]. Such issues are not rare because continuous flow has been utilized for decades in VADs. Thus, many scholars have proposed considerable schemes to generate pulsation flow, most of which achieved this purpose by developing variable rotation speed (VRS) [13,14].

However, none of them can be used on a blood pump, meaning there

* Corresponding author.

E-mail address: zhangxiw@tsinghua.edu.cn (X. Zhang).

is a need for control methods for blood pumps. Qian et al. [15] have proven that a pulsatile impeller pump has a more extensive free hemoglobin concentration than a nonpulsatile pump through animal experiments. Apparently, more complex boundary conditions may cause more substantial turbulence and higher shear stress, which are now considered the two main causes of blood cell damage [16]. Nevertheless, no explicit mechanism has been established to explain how it occurs. Thus, before setting out to form a pulsating flow in the microaxial blood pump, what will happen when variable speed is introduced needs to be studied.

In this research, we aim to determine the impact on the non-physiological shearing environment caused by altering speed, which is vital when considering hemolysis. Through CFD methods, more details are revealed to support experimental research. A pressure-based method is used to attain a pulsation flow, and the feedback process is not considered to simplify the calculation. By considering a pathology state, the analysis is more specific. Furthermore, we introduced a new criterion for assessing the fluid field under pulsating flow using turbulence analysis methods and compared the VRS and CRS results. The procedures are described in Fig. 1.

2. Materials and methods

2.1. The geometry model of the blood pump

A prototype of the microaxial blood pump was designed by the School of Aerospace, Tsinghua University, and has already been optimized through the Non-dominated Sorting Genetic Algorithms (NSGA-II). The aim of optimization is set to allow the pump to reach 60 mmHg with a flow capacity over 5 L/min and an efficiency over 60 %. As shown in Fig. 2, the prototype has an impeller with two blades, a diffuser with three blades and a thicker hub than the impeller, and a shroud that is placed around the complicated flow path formed by the structures previously mentioned.

It should be noted that the two blades of the impeller was shaped through a sweeping operation on two baselines: Baseline 1 and Baseline 2 as shown in Fig. 2. Baseline 1 is identical to the axial axis, while Baseline 2 can be described by the parametric equations below:

$$\begin{cases} t = \varphi r \\ x = r \cos \varphi \\ y = r \sin \varphi \\ z = at^3 + bt^2 + ct + d \end{cases} \quad (1)$$

where r is the radians of the impeller and φ is the angle under the polar coordinate system. The baseline (Baseline 2 in Fig. 2), which is used to generate the hub through the rotating operation, can be described as follows:

$$\begin{cases} z = ax^3 + bx^2 + cx + \eta \\ z|_{x=1.5mm} = 0 \end{cases} \quad (2)$$

The coefficients above, as well as other shape parameters, are shown in Table 1. The rated speed is set to 30,000 rpm.

2.2. Near physiology cardiovascular system model

Many scholars believe that blood pumps need to perform a pulsation flow during clinical usage. This means that a governing rule is essential, especially a physiology-guiding control strategy, which is generally either proposed through ECG or pressure boundaries [13,17]. The boundary conditions are usually set to be a pressure-inlet condition and a pressure-outlet condition, referring to similar studies. For the blood pumps mentioned above, the inlet condition should be the pressure of the left ventricle, while the outlet condition should be the pressure of the aorta. In this work, we will build a lumped parameter model to obtain the boundary conditions.

The microaxial blood pump aims to salvage cardiogenic shock and recover the patient's cardiac perfusion. Clinically, CS can be complicated, and there is no need to produce pulsating blood flow. Only patients who survive emergency treatment need pulsation blood flow assistance. However, there are few clinical follow-up cases of this blood flow condition, and data are difficult to obtain. Therefore, we fetched a case of a 78-year-old male patient with unstable angina pectoris (UAP) and myocardial hypertrophy who had just undergone heart bypass surgery within an hour before sampling. By collecting hemodynamic data, we obtained a similar pathological hemodynamic state of a treated CS patient. The raw data and aorta pressure (AOP) fitting function are shown in Fig. 3. AOP is estimated through radial artery pressure according to clinical physiology common sense. The fitting process was carried out by MATLAB® 2021 using the smoothing spline method, with the smoothing parameter set to 0.9. To save computing resources, only the second heartbeat cycle in the clinical dataset is selected here.

Due to the limitations of surgery, left ventricular pressure (LVP) is hard to measure. In this work, a heart simulation model is utilized to estimate the LVP. The heart model was constructed through a 5-circuit electric network, as shown in Fig. 4(A), which has already been commonly used to simulate the hemodynamics of the vascular system [18].

One hundred sample points are selected at the same moment in both the simulation and clinical datasets. The fitting process is performed by iteratively modifying the parameters of the elastic function and the electrical element model until the AOP is consistent with the clinical data. The criterion for consistency is that the Euclidean norm is within 10. Furthermore, the error between the minimum and maximum

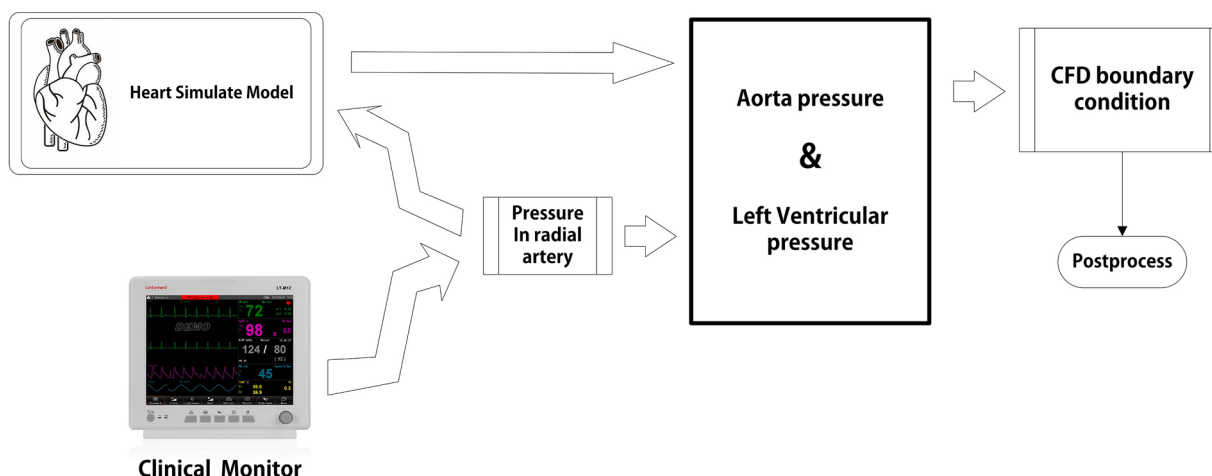


Fig. 1. Process of pathology state acquisition.

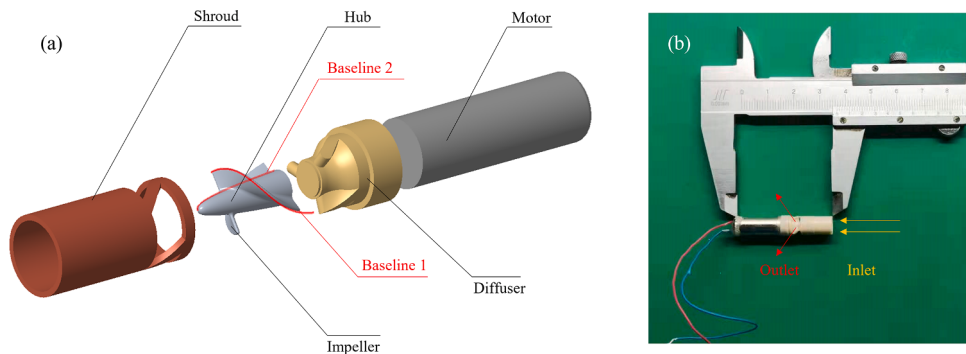


Fig. 2. The prototype for the blood pump (A) shows the main parts; Figure (B) shows the sample manufactured by Tsinghua University, which is used in experimental tests.

Table 1
Parameters for pump design.

Name	Final parameter	Units
r	2.80	mm
a	-1.65e-2	mm ⁻²
b	4.09e-2	mm ⁻¹
c	-5.70e-2	1
d	6.00	mm
α	-1.55	mm ⁻²
β	-1.71	mm ⁻¹
γ	2.44e-3	1
η	9.07	mm

pressure values is kept within 1 mmHg. This process is achieved through the genetic algorithm in which 50 samples are selected for the first generation and 50 generations are iterated.

In this model, according to Nikos et al. [19], heart beating was mimicked through a time-varying capacitance C(t), which is reciprocal to the myocardium compliance function E(t). The elastance function can be described as follows:

$$E(t) = (E_{max} - E_{min}) \times \left\{ a \left[\frac{\left(\frac{t}{\alpha_1 T} \right)^{n_1}}{1 + \left(\frac{t}{\alpha_1 T} \right)^{n_1}} \right] \times \left[\frac{1}{1 + \left(\frac{t}{\alpha_2 T} \right)^{n_2}} \right] \right\} + E_{min} \quad (3)$$

where the dimensionless numbers n_1 and n_2 characterize the steepness of ascending and descending, respectively, while α_1 and α_2 determine the appearance time of different components within one heartbeat period. Furthermore, all relative parameters are shown in Table 2. Other initial values of state variables and elements of the cardiovascular model, such as aortic valve resistance and systemic resistance, are referred from Zuo

et al. [20], as their model fits the myocardial hypertrophy.

It should be noted that while adjusting the parameters, we ensure that during the ejection period, LVP is slightly higher than AOP to prevent backflow during CFD computing. The early stage of the Simulink model calculation is not convergent, so sampling is selected after 5 heartbeat cycles; see Supplementary Materials for more details.

2.3. CFD model

According to the Frank-Starling mechanism, rotational speed alternation needs to fit the pressure condition as heart beating. High rotational speed is needed during systole to ensure ejection fraction [17], and a lower rotational speed is needed during diastole for suction prevention. Thus, varying CFD boundary conditions, rotational speed, inlet pressure, and outlet pressure need to be set. In this study, pressure boundaries are provided by the cardiovascular system model mentioned above. The rotational speed is set to vary from 27,000 rpm to 32,000 rpm according to the simulation data presented in Supplementary Materials, speed below 27,000 rpm cannot provide sufficient flow and pressure, and speed over 32,000 rpm will cause a decrease in efficiency. The constant rotational speed is set to 30,000 rpm according to the design proposal mentioned in Section 2.1. In this work, unlike many other studies, the controlling strategy uses a sigmoid function when increasing or decreasing the speed is needed. To implement this function, we presplit the heart-beating period into four parts, as shown in Fig. 4(B).

The setting of the rotational speed change is based on the cardiac model, as it can fit the physiological conditions of the patient. Specifically, the parameters of the Sigmoid function are determined by the parameters of the cardiac model, the expression is as follows:

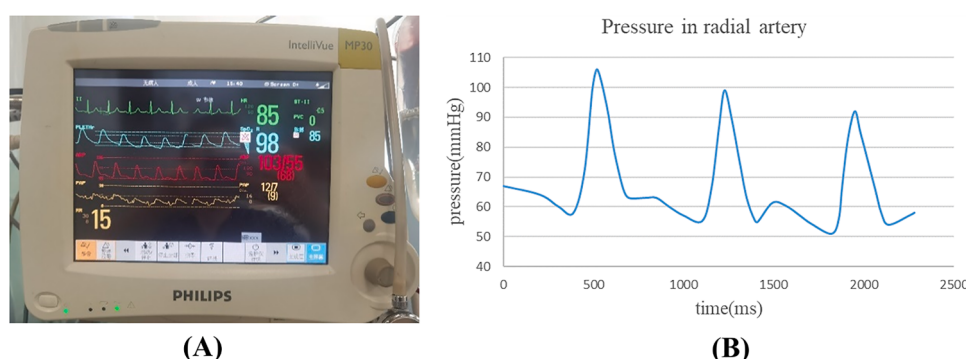


Fig. 3. Original clinic data (B) are the radial artery pressure fetched from the monitor in Figure (A), a PHILIPS® IntelliVue MP20/MP30 patient monitor.

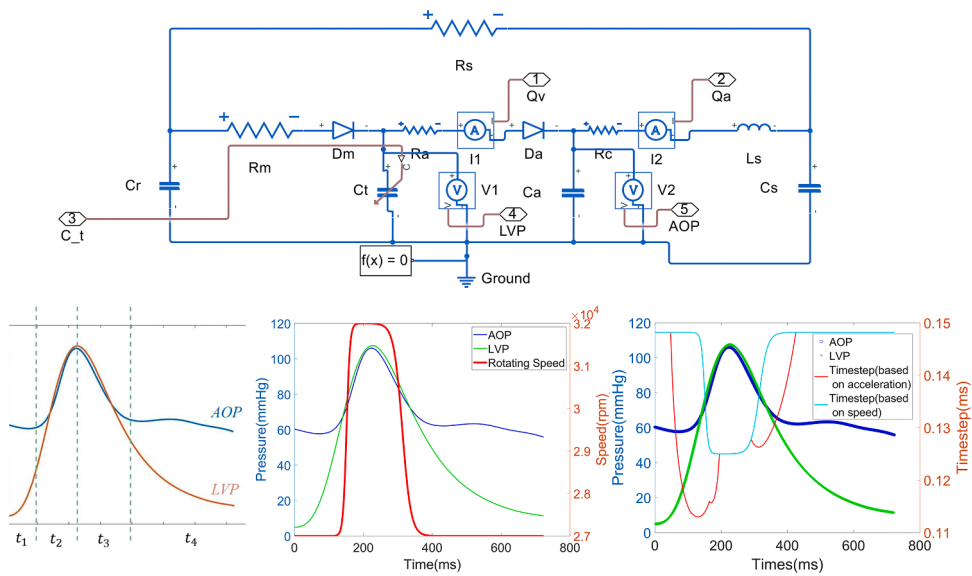


Fig. 4. Heart Model for the Patient. Figure (A) is the simulation circuit built in SIMULINK, Figure (B) shows the different periods in one heartbeat, which is used as segmentation criteria in speed setting, Figure (C) combines the rotational speed with pressure condition, and Figure (D) reveals the time step setting during calculation.

Table 2
Parameters for Heart Model.

Name	Final parameter	Description
n_1	2.3	The slope for the Systole period
n_2	4.3	The slope for the Diastole period
α_1	0.72	Time percentage for the Systole period
α_2	0.87	Time percentage for the Diastole period
E_{max}	1	maximum for compliance
E_{min}	0.025	minimum for compliance
α	1.55	Amplitude coefficient

$$speed = \begin{cases} N_{\min} & t \in [t_0, t_1] \\ \frac{N_{\max} - N_{\min}}{1 + \exp[\lambda_1 * (t - T_1)]} + N_{\min} & t \in [t_1, t_2] \\ \frac{N_{\max} - N_{\min}}{1 + \exp[\lambda_2 * (t - T_2)]} + N_{\min} & t \in [t_2, t_3] \\ N_{\min} & t \in [t_3, t_4] \end{cases} \quad (4)$$

$$\lambda_1 = -\frac{n_1}{n_2} \lambda_2 \quad T_1 = t_1 + \frac{t_2}{2} \quad T_2 = t_1 + t_2 + \frac{t_3}{2} \quad (5)$$

where λ_i reveals the rate for speed alternation and is related to the elastance function, as shown in Formula (5). N_{\max} and N_{\min} are the maximum and minimum of the speed. Here, $t_1=0.1058s$, $t_2=0.2058s$, $t_3=0.2424s$. The rotation speed function is shown in Fig. 4(C).

To maintain the accuracy of fluid simulation, the time step size should be strictly confined as in a single time step, and the physical state needs to be a quasisteady state. Here, we brought up two conceptions: one relates to the minimum rotation angle, the other relates to the rate of boundary condition variation. The more rapidly pressure or speed changes, the smaller time steps it requires. In addition, only the smaller one can be adopted. Then, the time step Δt can be described as:

$$\Delta t = \min \left\{ 0.1 * \exp \left[\frac{0.1}{\max \left(\frac{dLVP}{dt}, \frac{dAOP}{dt} \right)} \right], \frac{60}{N}, \frac{24}{360} \right\} \quad (6)$$

As the equation shows, the minimum rotation angle is set to 24° , which is a relatively accurate setting and will not cause too many computing source occupations. The distribution of time steps is shown in

Fig. 4(D).

A proper CFD setting for the prototype is needed before formal simulation. The steady flow state of the prototype has been computed by ANSYS® Fluent 2022, with the SST $k-\omega$ turbulence model and SIMPLE numerical method. The fluid field was generated by Boolean computation in Creo® 5.0. Tetrahedral meshing independency is tested to prove the irrelevance of setting methods on computing, presenting 5 million cells that could be accepted. Thus, 5.7 million cells and transient computing with the sliding mesh method were finally selected. Furthermore, the mesh generation was set to be multi sized to reveal more small geometry features, such as the gap between the impeller and shroud and the boundary layers of the impeller and diffuser. The meshing results are shown in Fig. 5.

Later, we experimented in vitro to verify the computation. The test loop, shown in Fig. 6(B), has a volume of approximately 4 L and has two pressure transmitters (NK CEMPX215, CHINA) and a precision ultrasonic flow meter (KEYENCE FD-X 10 mm Diameter, JAPAN). Water is chosen as the medium, the same as the CFD setting. A classic pump curve was compared with the CFD results in Fig. 6(A). The pressure heads were underpredicted at low flow rates, mostly because the motor drive of the prototype used in the experiment adopts an open-loop control strategy, the load on the blades is large at low flow rates, and will cause loss in rotational speed, but this does not affect the method and conclusion of this paper, as such a low flow rate will not be involved. Apart from this, although there is a small gap between the experiment and simulation due to systematic error, the CFD model's validation can still be trusted because it can still reveal the fluid process in the blood pump.

It should be noted that with the support of the pVAD, the pressure at the inlet and outlet of the pump may change as well. To verify whether the heart model described above will have changes in blood pressure after implantation of the blood pump, we fit the dynamic model of the blood pump with the CFD results described above and added it to the lumped parameter model. It was found that there was no significant change in pressure, which indicates that the cardiac model not only meets the pathological condition of the patient but also has similar hemodynamic conditions after assistance of pVAD. The comparison models can be found in the Supplementary Materials.

After that, the MATLAB Fluent_AAS toolbox is utilized to update Fluent's inlet and outlet pressure boundary conditions during the simulation, as mentioned in Section 2.3, the inlet condition is the pressure of the left ventricle, while the outlet condition is the pressure of

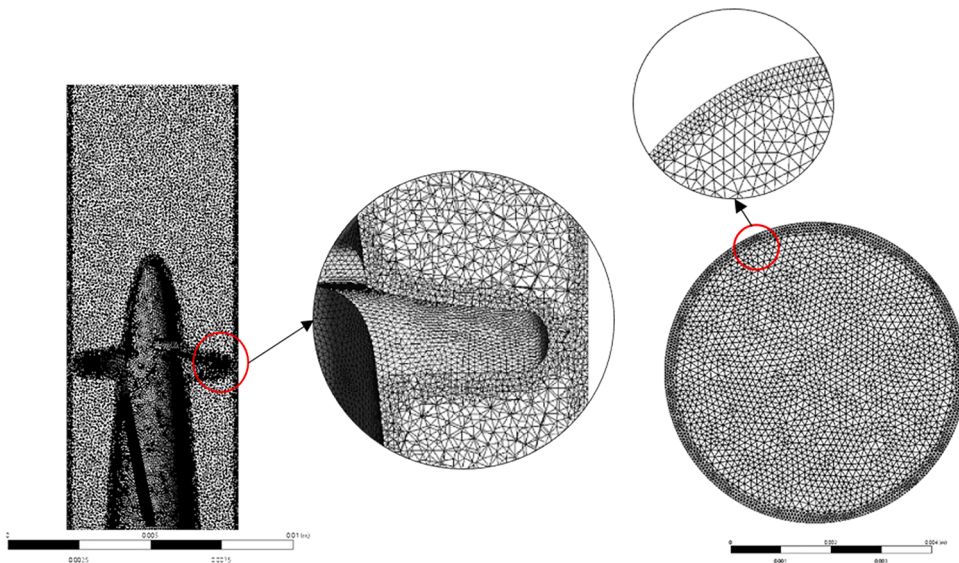


Fig. 5. Mesh details for the rotation region. The boundary layer near the impeller and the area of the flow gap have been refined to obtain a more accurate result.

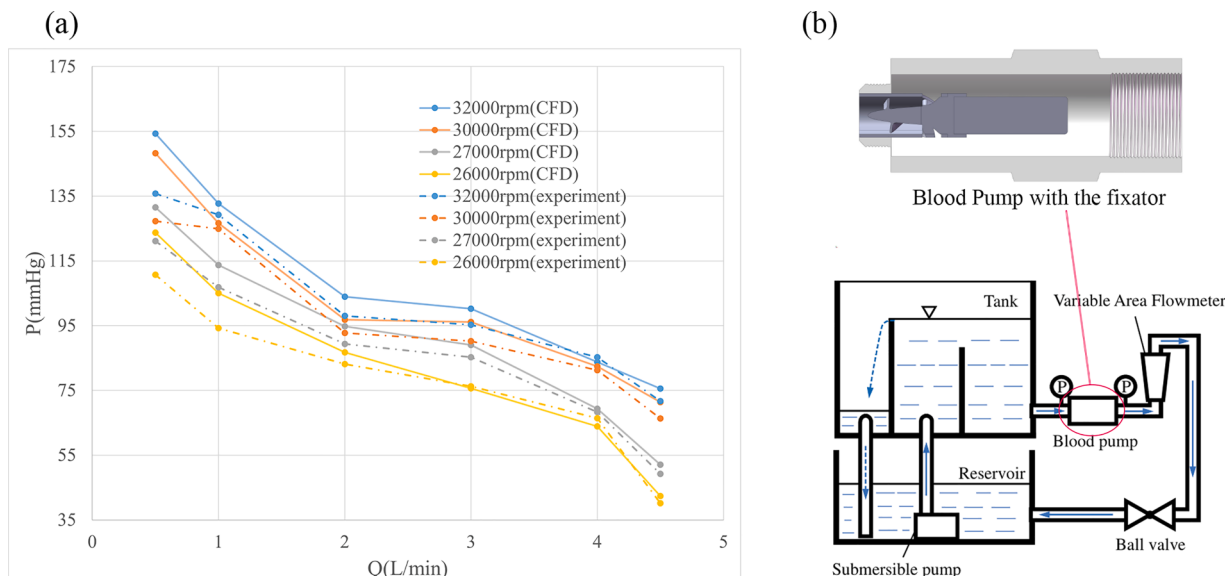


Fig. 6. Typical pump curve for the microaxial blood pump. Figure (A) and Figure (B) show the CFD and experimental results, indicating that the CFD results are reliable at speeds near 30,000 rpm and flow rates higher than 3 L/min. Figure (C) shows the sketch for the experiment facilities in this research, which was designed by Wu et al. [13].

the aorta. The updating code can also be found in the Supplementary Materials. In this case, the medium is blood instead of water. The density is set to 1050 kg/m^3 , and the viscosity is set to $0.0035 \text{ Pa}\cdot\text{s}$. The formal simulation with a transient model is carried out on a supercomputer in Beijing with CentOS Linux, using 60 cores of CPU; the computing continues until the continuous equation residual in each step is below 1×10^{-3} . More details about the CFD settings can be found in the Supplementary Materials.

2.4. Shear stress analysis and hemolysis prediction model

Hemolysis is a process in which red blood cells are destroyed, and the concentration of free hemoglobin (FHb) increases. There are many reasons for hemolysis, including genetic factors, abnormal blood osmotic pressure, and external nonphysiological mechanical stimulation. Using an artificial heart pump on patients inevitably increases the chance of physical contact between the blood and the solid surface of the

device, which will lead to mechanical red blood cell rupture. Furthermore, it induces a series of complications, such as hemolytic anemia, thrombosis, and renal failure. Therefore, it is necessary to evaluate the hemolysis. This evaluation method is quantized by a normalized variable called the hemolysis index (HI). In this paper, we suppose that the destruction of blood cells is due to shearing and a power-law model is adopted, the effect of turbulence is considered in the process of diffusion of free hemoglobin. The rate of turbulence dissipation will also affect hemolysis. But we won't take that into consideration for simplification. However, the analysis method in this paper can also be applied to other hemolysis prediction models like Wu et al.'s model [39]. Giersiepen et al. [21] proposed a model to describe the shearing process, which is calculated by:

$$H(\bar{\tau}, t) = \begin{cases} C\bar{\tau}^\alpha t^\beta & (\text{for } \bar{\tau} > \bar{\tau}_s) \\ 0 & (\text{for } \bar{\tau} \leq \bar{\tau}_s) \end{cases} \quad (7)$$

where C , α and β are constant parameters; referring to Ding et al. [22], the values are set as $C = 3.458 \times 10^{-6}$, $\alpha = 2.0639$, $\beta = 0.2777$, where $\bar{\tau}$ represents scalar stress and $\bar{\tau}_s$ is the threshold of hemolysis occurrence. Based on the tensor invariance, $\bar{\tau}$ is the scalar shear stress (SSS) based on invariants of the stress tensor and is described as:

$$\sigma_{ij} = 2\mu S_{ij}$$

$$\bar{\tau} = \left[\frac{1}{6} \sum_{i,j=1,2,3} (\sigma_{ii} - \sigma_{jj})^2 + \sum_{\substack{i,j=1,2,3 \\ i \neq j}} \sigma_{ij}^2 \right]^{\frac{1}{2}} \quad (8)$$

It should be noted that although the power-law-based hemolysis model cannot predict the free hemoglobin concentration accurately, it can still measure the hemocompatibility of blood pumps in different statuses, as well as the macro behaviors of hemoglobin; both of these aspects are vital for this research. Such a model has been used in numerous research and engineering cases. Thus, we still start from this model in this work.

The stress-based hemolysis model is typically used in Eulerian or Lagrangian methods. Zhang proved that in our blood pump, both types of analysis have little differences in underflow rates larger than 3 L/min. Thus, in this research, the Eulerian method is used, and the transport equation is:

$$\begin{aligned} \frac{\partial H_L}{\partial t} + \mathbf{v} \cdot \nabla H_L &= \delta C \bar{\tau}^{\frac{\alpha}{2}} (1 - H_L) \\ \delta &= \begin{cases} 0 & \text{if } \bar{\tau} < \bar{\tau}_s \\ 1 & \text{if } \bar{\tau} \geq \bar{\tau}_s \end{cases} \end{aligned} \quad (9)$$

2.5. Analysis of the transporting process

Turbulence is known to be a significant contributor to hemolysis [40]. Most studies have focused on the damaging effects of turbulence on red blood cells [26], yet the turbulence within any VAD can transport free hemoglobin along the streamline and cause accumulation. The hemolysis prediction model is described in the Eulerian method, and it can only predict hemolysis in the local control body. The FHB transported from other adjacent control bodies due to nonphysiology shearing has not yet been considered. In this work, we start with turbulence theories to determine which plays a more major role in local hemolysis, the effect of transportation or shearing stress.

The motion of turbulence is irregular; thus, it is a typical stochastic process. From the aspect of statistics, the motion of the fluid can be described as the Reynold Average Navier–Stokes (RANS) equation:

$$\frac{\partial u_i}{\partial t} + u_j \frac{\partial u_i}{\partial x_j} = -\frac{1}{\rho} \frac{\partial p}{\partial x_i} + \nu \frac{\partial^2 u_i}{\partial x_j \partial x_j} - \frac{\partial u'_i u'_j}{\partial x_j} + f_i \quad (10)$$

where u_i is the velocity, p is the pressure, ρ is the density, ν is the viscosity, and the symbol $\langle u \rangle$ is the average value. To be more detailed, we have the relationship:

$$\mathbf{u} = \langle \mathbf{u} \rangle + \mathbf{u}' \quad (11)$$

u' is the fluctuating quantity for variable u . Pulsation Navier–Stokes equation can be described as:

$$\begin{cases} \frac{\partial u'_i}{\partial t} + u_j \frac{\partial u'_i}{\partial x_j} + u'_j \frac{\partial u_i}{\partial x_j} = -\frac{1}{\rho} \frac{\partial p'}{\partial x_i} + \nu \frac{\partial^2 u'_i}{\partial x_j \partial x_j} - \frac{\partial}{\partial x_j} (u'_i u'_j - u'_i u'_j) \\ \frac{\partial u'_i}{\partial x_i} = 0 \end{cases} \quad (12)$$

Traditionally, hemolysis in VAD is considered mainly caused by shear stress, as shown in Section 2.4. To get more succinct, we transform

Eq. (9) to:

$$\frac{\partial H_L}{\partial t} + \mathbf{v} \cdot \nabla H_L = \delta C_0 \tau_0 (1 - H_L) \quad (13)$$

where $H_L = C \bar{\tau}^{\frac{\alpha}{2}} t = C_0 \tau_0 t$ means that hemolysis occurred locally, and then, taking the mean value for both sides, after simplification, we can obtain:

$$\frac{\partial H'_L}{\partial t} + u_i \frac{\partial H'_L}{\partial x_i} = \delta C_0 [\tau_0 (1 - H_L) - \tau'_0 H'_L] - \frac{\partial u'_i H'_L}{\partial x_j} \quad (14)$$

Subtracting Eq. (14) from Eq. (13), we can obtain the pulsation equation for hemolysis:

$$\begin{aligned} \frac{\partial H'_L}{\partial t} + u_i \frac{\partial H'_L}{\partial x_i} + u_i \frac{\partial H'_L}{\partial x_i} \\ = \delta C_0 (\tau'_0 - H'_L \tau_0 - \tau'_0 H_L - \tau'_0 H'_L + \tau'_0 H'_L) - \frac{\partial}{\partial x_i} (u'_i H'_L - u'_i H'_L) \end{aligned} \quad (15)$$

Put $H_L = C_0 \tau_0 t$ into this equation to simplify:

$$\frac{(1-\delta)\tau'_0}{t} + u'_i \frac{\partial \langle \tau_0 \rangle}{\partial x_i} + \langle u'_i \rangle \frac{\partial \tau'_0}{\partial x_i} = \delta C_0 \left(\langle \tau'^2_0 \rangle - 2\tau'_0 \langle \tau_0 \rangle - \tau'^2_0 \right) - \frac{\partial}{\partial x_i} (u'_i \tau'_0 - \langle u'_i \tau'_0 \rangle) \quad (16)$$

From the equation above, if processing integral on time and space, we can obtain the strain energy performed on hemolysis. Here, τ_0 can be seen as energy under unit time and unit volume or unit hemolysis energy. The left side of the equation describes the variation in average quantities. This kind of variation is contributed by two parts: the first item on the right side described pure stress results, while the second item described an extra contribution to fluid transport and shear stress. This means that in addition to the diffusion of hemoglobin, the movement of turbulence will transport hemoglobin to another controlling body. Details about the derivation process can also be found in the Supplementary Materials.

By combining Eqs. (11) and (15), we can obtain the pulsation hemolysis describing equations; similarly, we should consider the Reynold hemolysis item. Eq. (16) can be concluded as two parts: H_R reveals the diffusion effect, and τ_R reveals the shear effect.

$$H_R = C_0 \sum u'_i \tau_0 \Delta t \quad (17)$$

$$\tau_R = \left(\langle \tau'^2_0 \rangle - 2\tau'_0 \langle \tau_0 \rangle - \tau'^2_0 \right) \quad (18)$$

3. Results and fluid field analysis

The results and the following analysis are presented in three parts: (1) The hemodynamic performance, which offers an overview of the results. (2) The shear stress environment and details in fluid fields analyzing and assessing how much the SSS affects the hemolysis. (3) The proper orthogonal decomposition (POD) analysis is processed on H_R and τ_R , which reveals the mechanism of how instability affects hemolysis.

3.1. Hemodynamic and hemolysis results

The hemodynamic states for VRS and CRS are shown below in Fig. 7 (A). As shown, both control methods significantly gain cardiac output and finally reach an expected output of 65 ml per heartbeat. Although the increase produced by both methods is approximately the same, the VRS has a better pulsation characteristic (Fig. 7(B)), as the range of the output flow rate is more comprehensive in VRS. The results in Fig. 7(B) are similar to the results of existing experiments [23]. This proves that the simulation results in this paper are macroscopically credible.

Then, the volume average of HI at different moments is calculated (Fig. 7(C)). The local hemolysis production in VRS is undulatory after an increment, while CRS increases first and then maintain increases.

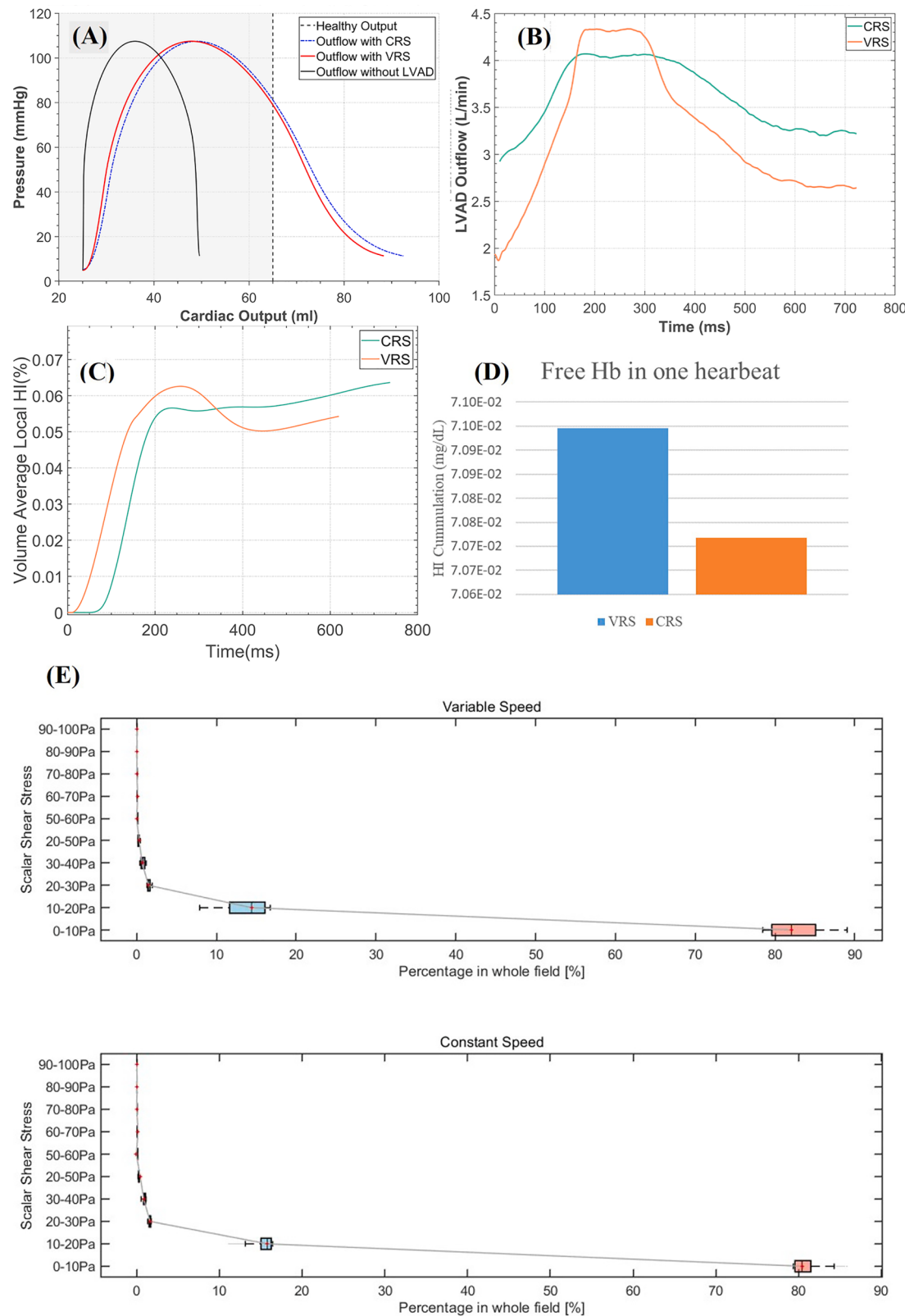


Fig. 7. The main results of hemodynamics. Figure (A) shows the total heart output and the pressure variation in the LV. Figure (B) is the outflow contributed by LVAD under two different speed settings. Figure (C) and Figure (D) are the results of HI. One is the local average, and the other is the total. Figure (E) is the distribution of SSS.

Interestingly, when referring to the accumulation of free hemoglobin, we found a slight increase from CRS to VRS by approximately 4.2 %, which is not as expected (Fig. 7(D)). From one aspect, the equivalent speed for VRS is nearly 2000 rpm lower than CRS, which means that less work applied on the blood means less damage to the red blood cell. Yet VRS causes a little more hemolysis, which may be caused by instability in VRS. From another aspect, the difference would be widened when considering a more extended period by estimating a 1.35 mg/dl rise per hour. Other extra hemolysis, such as that caused by blood clots under VRS, may also exist [24]. Despite all the above, the disparity between VRS and CRS in the hemolysis of pVAD is not conspicuous enough compared to traditional long-term VADs [25].

Furthermore, we calculated the SSS distribution during different time steps to discuss the shear environment differences (Fig. 7(E)). By counting the percentage of volume corresponding to different SSS ranges, it is evident that shear stresses between 0 Pa and 20 Pa mainly account for 90 % of the volume of the whole area in both cases. For VRS, the spatial distribution of SSS varies more. Because of the small size of the blood pump and high rotational speed, the output is more sensitive to rotational speed. Thus, the change in rotational speed in VRS does not exceed 7 % of the average speed, while in traditional long-term VADs, it can be near 15 % [25].

It should be noted that a precalculation was carried out to obtain a relatively steady flow state before boundary condition changes. However, HI at the beginning can be different due to different precalculation times. This is not a problem, as the HI here calculates only the initial local data, and while discussing hemolysis accumulation, the initial quantity is subtracted.

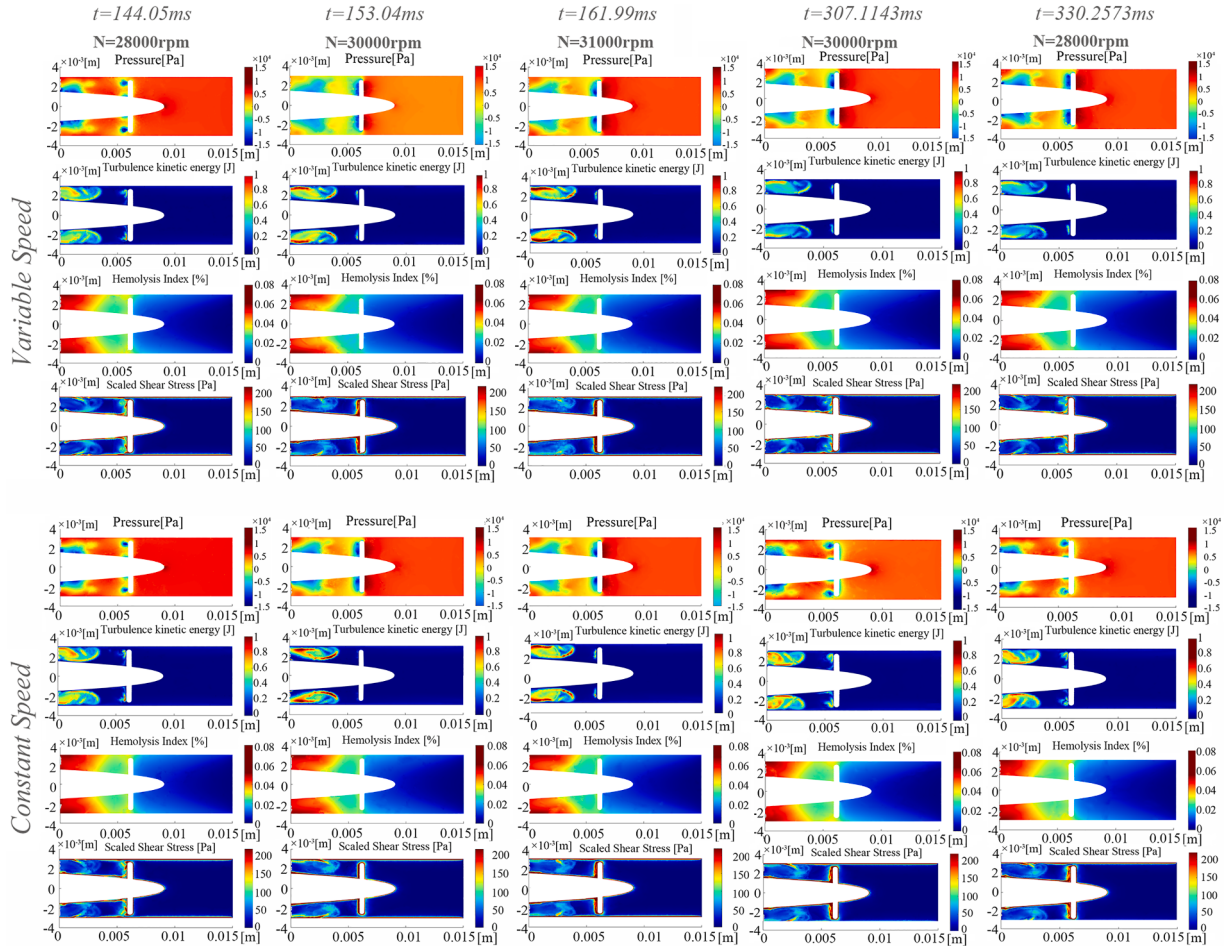


Fig. 8. Contour plot for the four factors: pressure, turbulence kinetic energy (TKE), hemolysis, and SSS. The first row shows the results of pressure, the second turbulence kinetic energy, the third one HI and the last SSS. The results in the same row have the same color bar as well.

3.2. Flow state and hemolysis spatial distribution

This section will discuss four main factors in space: pressure, turbulence kinetic energy (TKE), hemolysis, and SSS, as well as the potential relationship among them. A specific plane was chosen to examine the variation of different quantities. The plane ensures that the position of the impeller is the same in each sampling. The influence caused by boundary conditions at different moments is separated by choosing the same time spot in VRS and CRS.

From Fig. 8, the following rules can be summarized:

- The change in the pressure field is mainly reflected in the expansion and contraction of the low-pressure area, which is dominated by both the boundary conditions and the speed. In VRS, as the rotational speed changes, the expansion rate of the low-pressure region is higher during acceleration or deceleration.
- In the VRS, the TKE clearly shows a trend of strengthening first and then weakening, while in the CRS, it appears to be strengthening continuously.
- The high shearing zone lies near the wall in both cases. In VRS, the SSS forms an arc-shaped sub high region, and as the speed increases, it moves toward the wall of the shroud. As the impeller slows down, it differentiates another arc. In CRS, the differentiated arc is not conspicuous and appears only at the highest and lowest speeds.
- For the hemolysis area, we found that for VRS, there is a tendency to push forward in the high hemolytic region in the middle of the leaf, while CRS does not.

Pressure, TKE and SSS are seen as the reasons for hemolysis by many studies [26–28]. The conclusions above tell us that hemoglobin accumulates in VRS, which is caused by the instability of these factors. It is mainly reflected in shear instability and flow instability. The mechanism needs to be investigated further.

It should be noted that there are many other potential reasons, such as the scale of vortexes. It is said that vortices with the Kolmogorov scale close to the diameter of blood cells will increase the destruction of blood cells [27]. However, in this work, we will not discuss them much because they require a more detailed calculation, such as DNS. Instead, we will discuss how shear stress and shearing deuced transporting affect hemoglobin distribution by comparing H_R and τ_R discussed in Section 2.5.

3.3. Unsteady flow state and its contribution to hemolysis

Hemodynamics analysis can explain the effects of nonphysiological shear stress from one aspect. In both cases, the distribution of SSS is approximately the same, although the percentage of SSS below 20 Pa in VRS is slightly higher than that in CRS as shown in Fig. 7(E). Thus, the reason for the increment in hemolysis falls upon fluid instability, and the flow state needs to be analyzed further.

The POD [29] method is commonly used in turbulence analysis, and such a method has also been used in pump studies [30,31]. In this work, the POD process is used in analyzing H_R and τ_R . The fluctuation quantities will be decomposed into an orthonormal system of POD basis function φ_j and POD temporal coefficient a_j , as shown in Eq. (19).

$$\mathbf{q}(\mathbf{x}, t_i) = \sum_{j=1}^m \mathbf{a}_j(t_i) \cdot \varphi_j(\mathbf{x}) \quad (19)$$

By forming a square matrix A in Eq. (20), we can obtain its eigenvalues λ_i and its corresponding eigenvector. Then, we can calculate φ_j and a_j in Eq. (21).

$$\begin{cases} \mathbf{P} = [\mathbf{q}(\mathbf{x}, t_1), \mathbf{q}(\mathbf{x}, t_2), \dots, \mathbf{q}(\mathbf{x}, t_m)] \\ \mathbf{A} \mathbf{Q}_j = \lambda_j \mathbf{Q}_j \end{cases} \quad (20)$$

$$\varphi_j = \frac{\mathbf{P} \mathbf{Q}_j}{\sqrt{\lambda_j}} \mathbf{a}_j = \varphi_j^T \mathbf{P} \quad (21)$$

where a_j is a row vector arranged in time series, reflecting the temporal characteristic of the j th POD mode; φ_j is a column vector corresponding to the grid nodes, reflecting the spatial distribution of the j th POD mode. The POD eigenvalue calculated from Eq. (20) signifies the perturbation energy of the POD mode.

Before processing POD, a consensus needs to be reached. In this paper, as mentioned above, the RANS method has been used in CFD computing, meaning that the results calculated within each time step follow one hypothesis: flow is seen as a constant flow during one step. Therefore, the solution result is already time-averaged, and the variables \bar{u}_i and \bar{v}_i represent average spatial quantities. Afterward, the fluctuation for H_R and τ_R established in Section 2.5 can be obtained. To reveal more information about the 3-dimensional results, four sketches are set along the axial direction z , with a spacing of 2.5 mm, representing four regions

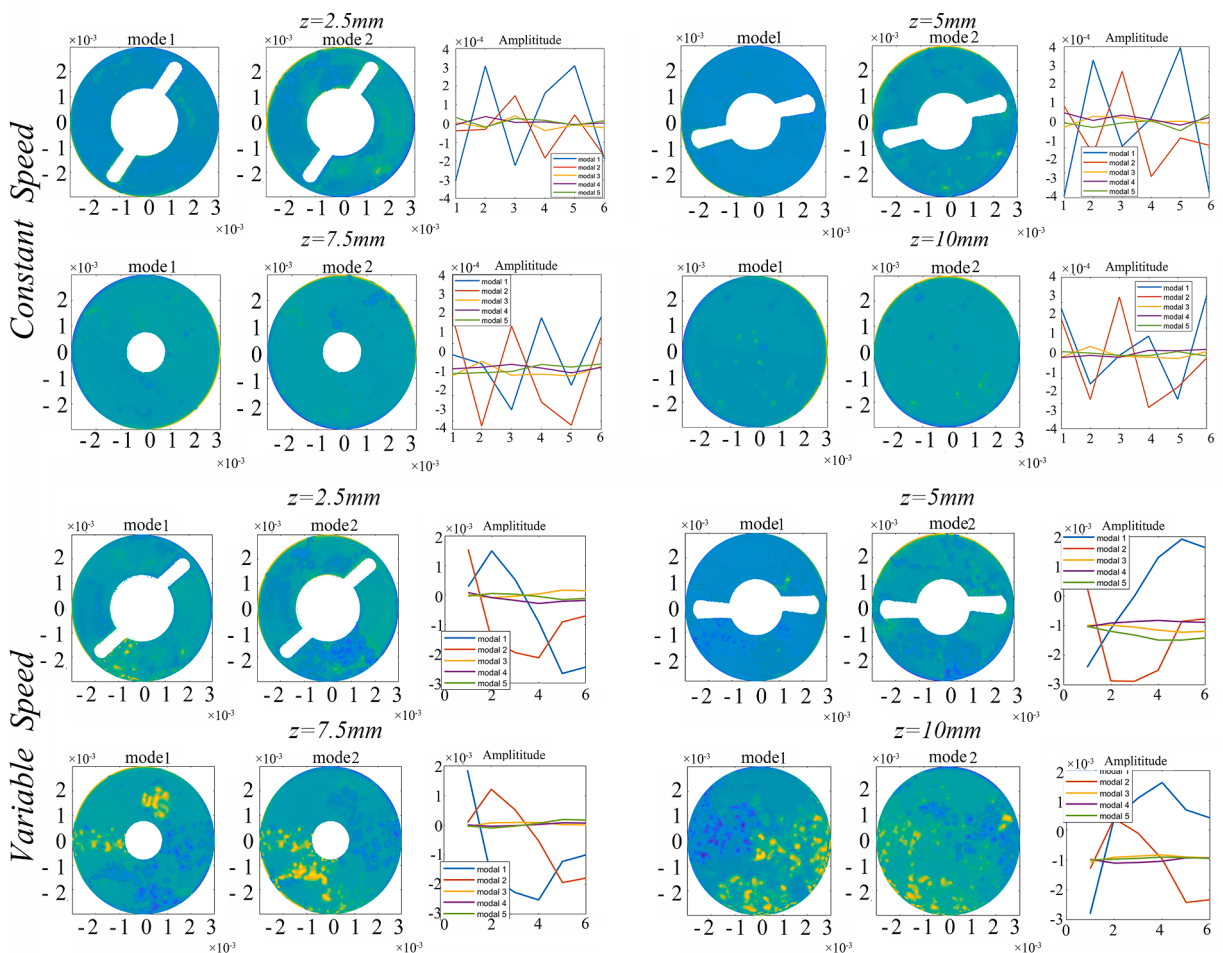


Fig. 9. POD results on H_R for VRS and CRS; 4 locations are considered: $z=2.5$ mm, $z=5$ mm, $z=7.5$ mm and $z=10$ mm.

of interest: a region without an impeller, a region with a hub only, a region with a hub and blades and an area near the outlet. The results are shown in Figs. 9 and 10. The energy distribution is described in Table 3 below, and the first five modes can be considered, as they can cover over 95 % of the total energy.

By comparing the energy distribution in Table 3, it can be concluded that the first two modes within five modes mainly occupy the total energy in both cases. As the sketch moves away from the bottom of the impeller, the energy of the first mode begins decreasing. In addition, the first mode of CRS has higher energy than VRS, meaning that CRS is mainly determined by the first mode and has less complexity. In Figs. 9 and 10, only the first and second modes are presented. More other results can be found in the Supplementary Materials.

The description above only considers spatial information, as for the time information, a fast Fourier transform (FFT) is commonly used to analyze the changes in amplitude over time to obtain the frequency information [32]. However, according to the time-step setting discussed in Section 2.3, the nonuniform method causes trouble in frequency information extraction. Hence, the FFT is not implemented. Instead, only amplitudes at certain moments identical to those in Section 3.2 are shown. The more fluctuation occurs in the high-energy mode, the more unstable the local flow state is.

In Fig. 9, POD is processed on H_R . It is not hard to determine that the fluctuation occurs much more in VRS. The fluctuation phenomenon is concentrated in the low-pressure area on the back of the blade. There is no apparent concentration at parts that do not involve the impeller. The changes in the amplitude of modes 1 and 2 as the location shifts are

noticeable. In VRS, modal 1 has more obvious alternation. In CRS, modal 1 exhibits a more similar frequency. Therefore, we can conclude that in VRS, the complexity of fluid has higher energy, and Reynold Hemolysis transports faster from locations without rotor to downstream than CRS.

In Fig. 10, POD is processed on τ_R . Similar to H_R , in VRS, the fluctuation phenomenon is concentrated in the low-pressure area on the back of the blade in regions with an impeller. There is no apparent concentration at parts that do not involve the impeller. The main differences between H_R and τ_R can be found in CRS. Unlike VRS, CRS has a significant fluctuation phenomenon in regions without the rotor and concentrates near the shroud wall. This means that the pulsation phenomenon of shear stress exists in both CRS and VRS, and VRS only makes this phenomenon enhanced. The phenomenon of hemoglobin transport only exists in VRS. For the amplitudes of different modes in both cases, CRS changes little over time, which is contrary to VRS.

In summary, shearing and turbulence play roles in FHb accumulation. Especially in the blade area. When VRS is introduced in the area without the rotator, instability plays a more prominent role through transplanting FHb. Such instability also affects the shearing environment, which explains why VRS has a more comprehensive SSS magnitude range than CRS.

4. Discussion and conclusion

In this paper, two microaxial blood pump control methods are performed in silico. The primary purpose is to determine whether the potential for extra hemolysis exists when the speed of the blood pump is

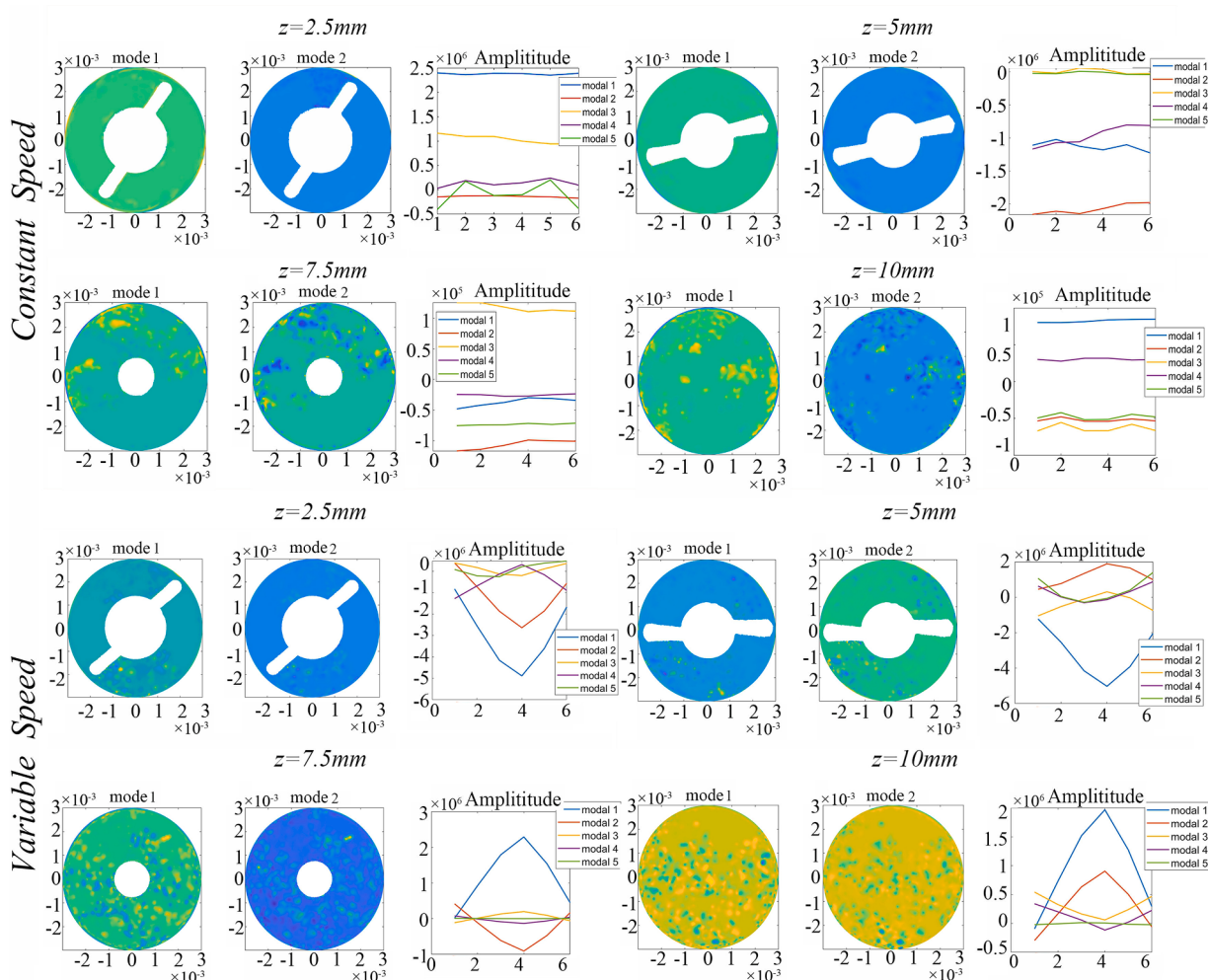


Fig. 10. POD results on τ_R for VRS and CRS; 4 locations are considered: $z=2.5$ mm, $z=5$ mm, $z=7.5$ mm and $z=10$ mm.

Table 3

Energy distribution for the first five modal at different sketches (%).

H_R	CRS				VRS			
distance (mm)	$z=2.5$	$z=5$	$z=7.5$	$z=10$	$z=2.5$	$z=5$	$z=7.5$	$z=10$
mode 1	66.14	63.32	52.96	50.07	63.79	58.98	47.21	51.96
mode 2	30.25	33.38	45.21	48.44	26.81	29.99	42.97	38.22
mode 3	0.94	0.68	0.68	0.43	3.15	3.37	3.89	4.15
mode 4	0.46	0.52	0.37	0.28	1.18	2.18	2.99	2.28
mode 5	0.40	0.50	0.32	0.21	0.86	0.92	0.49	0.40
τ_R	CRS				VRS			
distance (mm)	$z=2.5$	$z=5$	$z=7.5$	$z=10$	$z=2.5$	$z=5$	$z=7.5$	$z=10$
mode 1	71.64	65.61	52.78	55.15	62.63	54.02	70.75	65.02
mode 2	7.80	13.98	12.53	10.80	20.33	22.38	11.34	16.62
mode 3	6.66	6.07	9.75	8.70	4.53	6.20	3.68	4.66
mode 4	2.85	3.80	7.08	7.74	2.31	3.71	2.25	2.56
mode 5	1.97	1.80	5.80	6.19	1.58	2.00	2.04	1.52

altered. Three levels of analysis are carried out:

- (1) The performance on hemodynamics predicts that VRS will cause an increase in HI but is not disparate. This is contrary to the conclusion of conventional ventricular assist devices, especially in centrifugal pumps, who report that VRS has an approximately 30 % rise in hemolysis [33–35], which is much more than the conclusion here. This could be evidence that variable speed control can be used in pVAD and may not cause significant free hemoglobin accumulation.
- (2) Hemoglobin accumulates in VRS, which is caused by the instability of shear stress and flow state.
- (3) In the blade area, the mechanism of action of VRS and CRS is the same. When VRS is introduced in the area without the rotator, instability plays a more prominent role through transplanting FHb.

There may be a distinction between the experimental results, although there is still no report on a similar case. Research [36,37] has proven that the extra free hemoglobin environment may exceed the neutralizing ability of haptoglobin, which means that more transportation may increase the kidney burden. This should be taken into account during control strategy and impeller shape design. In addition to effects on terminal organs, it has also been reported that unsteady flow regions, or even turbulent regions of VADs, are the underlying cause of device-induced bleeding. [38]

Certainly, inadequacies exist in this work. There is still room for improvement in the level of meshing when more computational sources are introduced and more details can be witnessed. Furthermore, with a better or even structured mesh, the LES model can be employed, and details on the vortex may be revealed more. For the boundary condition, the pressure state in the left ventricle is an approximation, and both boundaries may not have a uniform pressure distribution. Thus, a better measurement may make the results more realistic.

In future research, those defects will be amended, and a new series of experimental facilities will be designed to perform a test on the hemolytic condition for both CRS and VRS and then verify the conclusion in this research.

Declaration of Competing Interest

The authors declare that they have no known competing financial interests or personal relationships that could have appeared to influence the work reported in this paper.

Acknowledgements

This work was supported by the National Key R&D Program of China

(Grant No. 2022YFC2402600) and National Natural Science Foundation of China (Grant No. 11972215, 12072174).

Supplementary materials

Supplementary material associated with this article can be found, in the online version, at [doi:10.1016/j.cmpb.2023.107919](https://doi.org/10.1016/j.cmpb.2023.107919).

References

- [1] R.L. Kormos, L.W. Miller, *Mechanical Circulatory Support – A Companion to Braunwald's Heart Disease*, Elsevier, Philadelphia, 2020.
- [2] A. Le Guyader, M. Pernot, C. Delmas, et al., Budget Impact associated with the introduction of the impella 5.0® mechanical circulatory support device for cardiogenic shock in France, *Clinicoecon Outcomes Res* 13 (2021) 53–63, <https://doi.org/10.2147/CEOR.S278269>.
- [3] Writing committee of the report on cardiovascular health and diseases in China, Report on cardiovascular health and diseases in China 2021: an updated summary, *Biomed Environ Sci* 35 (7) (2022) 573–603, <https://doi.org/10.3967/bes2022.079>.
- [4] B. Alushi, A. Douedari, G. Froehlig, W. Knie, T.H. Wurster, D.M. Leistner, B. E. Stahli, et al., Impella Versus IABP in acute myocardial infarction complicated by cardiogenic shock, *Open Heart* 6 (1) (2019), e000987, <https://doi.org/10.1136/openhrt-2018-000987>.
- [5] K. Frain, P. Rees, Intra-aortic balloon pump versus percutaneous Impella® in emergency revascularisation for myocardial infarction and cardiogenic shock: systematic review, *Perfusion* (2021), 2676591211037026, <https://doi.org/10.1177/02676591211037026>.
- [6] Kuno T., H. Takagi, T. Ando, M. Safety and efficacy of mechanical circulatory support with impella or intra-aortic balloon pump for high-risk percutaneous coronary intervention and/or cardiogenic shock: insights from a network meta-analysis of randomised trials. *Catheter Cardiovasc Interv* 97, no. 5: E636–E45. [10.002/cdd.29236](https://doi.org/10.002/cdd.29236).
- [7] F. Pappalardo, C. Schulte, M. Pieri, B. et al., Concomitant implantation of impella (R) on top of veno-arterial extracorporeal membrane oxygenation may improve survival of patients with cardiogenic shock, *Eur J Heart Fail* 19 (3) (Mar 2017) 404–412, <https://doi.org/10.1002/ejhf.668>.
- [8] J.R. Spratt, G. Ravveendran, K. Liao, Novel percutaneous mechanical circulatory support devices and their expanding applications, *Expert Rev Cardiovasc Ther* 14 (10) (2016) 1133–1150, <https://doi.org/10.1080/14779072.2016.1214573>.
- [9] A.N. Vora, W.Schuyler Jones, A.D. DeVore, A. Ebner, W. Clifton, M.R. Patel, First-in-Human Experience with Aortix Intraaortic Pump, *Catheter Cardiovasc Interv* 93 (3) (2019) 428–433, <https://doi.org/10.1002/cdd.27857>.
- [10] Y. Li, Y. Xi, H. Wang, A. Sun, X. Deng, Z. Chen, Y. Fan, The impact of a new arterial intravascular pump on aorta hemodynamic surrounding: a numerical study, *Bioengineering* 9 (10) (2022), <https://doi.org/10.3390/bioengineering9100547> (Basel)Oct 13.
- [11] N. Moazami, W.P. Dembitsky, R. Adamson, et al., Does pulsatility matter in the era of continuous-flow blood pumps? *J. Heart Lung Transpl.* 34 (8) (2015) 999–1004, <https://doi.org/10.1016/j.healun.2014.09.012>.
- [12] H. Liu, S. Liu, X. Ma, Varying speed modulation of continuous-flow left ventricular assist device based on cardiovascular coupling numerical model, *Comput Methods Biomech Biomed Engin* 24 (9) (2021) 956–972, <https://doi.org/10.1080/10255842.2020.1861601>.
- [13] Wu Xiao, Xiwen Zhang, Pengfei Hao, Feng He, Comparison of three control strategies for axial blood pump, *J. Mech. Med.Biol.* 19 (06) (2019), <https://doi.org/10.1142/s0219519419500581>.
- [14] T. Jing, T. Xin, F. Wang, Z. Zhang, L. Zhou, Control strategy design of a microblood pump based on heart-rate feedback, *Micromachines* 13 (3) (2022), <https://doi.org/10.3390/mi13030358> (Basel).

- [15] K.X. Qian, Q. Fei, Haemolysis test of non-pulsatile and pulsatile impeller blood pumps, *Clin Phys Physiol Meas* 9 (2) (1988) 107–112, <https://doi.org/10.1088/0143-0815/9/2/002>.
- [16] James Madison, D. Papavassiliou, E. O'Rear, Use of computational fluid dynamics to analyse blood flow, hemolysis and sublethal damage to red blood cells in a bileaflet artificial heart valve, *Fluids* 4 (1) (2019), <https://doi.org/10.3390/fluids4010019>.
- [17] S. Bozkurt, Physiologic outcome of varying speed rotary blood pump support algorithms: a review study, *Austr. Phys. Eng. Sci. Med.* 39 (1) (2016) 13–28, <https://doi.org/10.1007/s13246-015-0405-y>.
- [18] K.E. Tan, S. Yahya, H.A.F. Almurib, M. Moghavvemi, Modelling of human cardiovascular system in ventricular assist device simulation, in: Proceedings of the IEEE Industrial Electronics and Applications Conference (IEACon), Kota Kinabalu, Malaysia, 2016, pp. 304–311, <https://doi.org/10.1109/IEACON.2016.8067396>.
- [19] N. Stergiopoulos, J.J. Meister, N. Westerhof, Determinants of stroke volume and systolic and diastolic aortic pressure, *Am. J. Physiol.* 270 (6) (1996) H2050–H2059, <https://doi.org/10.1152/ajpheart.1996.270.6.H2050>. Pt 2.
- [20] X. Zuo, et al., Co-simulation of hypertensive left ventricle based on computational fluid dynamics and a closed-loop network model, *Comput. Methods Progr. Biomed.* 216 (2022), 106649, <https://doi.org/10.1016/j.cmpb.2022.106649>.
- [21] M. Giersiepen, L.J. Wurzinger, R. Opitz, H. Reul, Estimation of shear stress-related blood damage in heart valve prostheses - in vitro comparison of 25 aortic valves, *Int. J. Artif. Organs* 13 (5) (1990) 300–306, <https://doi.org/10.1177/039139889001300507>.
- [22] J. Ding, S. Niu, Z. Chen, T. Zhang, B.P. Griffith, Z.J. Wu, Shear-induced hemolysis: species differences, *Artif. Organs* 39 (2015) 795–802, <https://doi.org/10.1111/aor.12459>.
- [23] D. Rüschen, M. Rimke, J. Gesenhues, S. Leonhardt, M. Walter, Online cardiac output estimation during transvalvular left ventricular assistance, *Comput. Methods Progr. Biomed.* 171 (2019) 87–97, <https://doi.org/10.1016/j.cmpb.2016.08.020>.
- [24] Y. Hernaningsih, J.S. Akualing, The effects of hemolysis on plasma prothrombin time and activated partial thromboplastin time tests using photo-optical method, *Medicine* 96 (38) (2017) e7976, <https://doi.org/10.1097/MD.0000000000007976> (Baltimore).
- [25] F. Huang, H. Lei, S. Ying, Numerical hemolysis performance evaluation of a rotary blood pump under different speed modulation profiles, *Front. Physiol.* 14 (2023), <https://doi.org/10.3389/fphys.2023.1116266>.
- [26] M.M. Faghih, M.K. Sharp, Modeling and prediction of flow-induced hemolysis: a review, *Biomech. Model. Mechanobiol.* 18 (4) (2019) 845–881, <https://doi.org/10.1007/s10237-017-0995-2>.
- [27] M. Ozturk, E.A. O'Rear, D.V. Papavassiliou, Hemolysis related to turbulent Eddy size distributions using comparisons of experiments to computations, *Artif. Organs* 39 (12) (2015) E227–E239, <https://doi.org/10.1111/aor.12572>.
- [28] C.S. Jhun, M.A. Stauffer, J.D. Reibson, et al., Determination of reynolds shear stress level for hemolysis, *ASAIO J.* 64 (1) (2018) 63–69, <https://doi.org/10.1097/0000000000000615>.
- [29] K. Taira, S.L. Brunton, S.T.M Dawson, Modal analysis of fluid flows: an overview, *AIAA J.* 55 (12) (2017) 4013–4041, <https://doi.org/10.2514/1.J056060>.
- [30] Z.Y. Liao, J. Yang, X.H. Liu, W.L. Hu, X.R. Deng, Analysis of unsteady flow structures in a centrifugal impeller using proper orthogonal decomposition, *Journal of Appl. Fluid Mech.* 14 (01) (2021), <https://doi.org/10.47176/jafm.14.01.31299>.
- [31] X.B. Chen, R.H. Zhang, W.F. Yang, Inverse design and optimization of low specific speed centrifugal pump blade based on adaptive POD hybrid model, *J. Appl. Fluid Mech.* 15 (2) (2022), <https://doi.org/10.47176/jafm.15.02.33031>.
- [32] C.W. Rowley, S.T.M. Dawson, Model reduction for flow analysis and control, *Annu. Rev. Fluid Mech.* 49 (1) (2017) 387–417, <https://doi.org/10.1146/annurev-fluid-010816-060042>.
- [33] Z. Chen, S.K. Jena, G.A. Giridharan, S.C. Koenig, M.S. Slaughter, B.P. Griffith, Z. J. Wu, Flow features and device-induced blood trauma in cf-vads under a pulsatile blood flow condition: a CFD comparative study, *Int. J. Numer. Method Biomed. Eng.* 34 (2) (2018), <https://doi.org/10.1002/cnm.2924>.
- [34] Wang Yiwen, Peng Shen, Minli Zheng, Pengqiang Fu, Lijia Liu, Jingyu Wang, Lishan Yuan, Influence of impeller speed patterns on hemodynamic characteristics and hemolysis of the blood pump, *Appl. Sci.* 9 (21) (2019), <https://doi.org/10.3390/app9214689>.
- [35] L. Wiegmann, B. Thamsen, D. de Zelincourt, M. Granegger, S. Boes, M. Schmid Daners, M. Meboldt, V. Kurtcuoglu, Fluid dynamics in the heartmate 3: influence of the artificial pulse feature and residual cardiac pulsation, *Artif. Organs* 43 (4) (2019) 363–376, <https://doi.org/10.1111/aor.13346>.
- [36] D.J. Schaer, P.W. Buehler, A.I. Alayash, J.D. Belcher, G.M. Vercellotti, Hemolysis and free hemoglobin revisited: exploring hemoglobin and heme scavengers as a novel class of therapeutic proteins, *Blood* 121 (8) (2013) 1276–1284, <https://doi.org/10.1182/blood-2012-11-451229>.
- [37] D.J. Schaer, F. Vinchi, G. Ingoglia, et al., Haptoglobin, hemopexin, and related defense pathways-basic science, clinical perspectives, and drug development, *Front. Physiol.* 5 (2014) 415, <https://doi.org/10.3389/fphys.2014.00415>.
- [38] Y. Li, H. Wang, Y. Xi, et al., A mathematical model for assessing shear induced bleeding risk, *Comput. Methods Programs Biomed.* 231 (2023), 107390, <https://doi.org/10.1016/j.cmpb.2023.107390>.
- [39] P. Wu, S. Groß-Hardt, F. Boehning, et al., An energy-dissipation-based power-law formulation for estimating hemolysis, *Biomech. Model. Mechanobiol.* 19 (2) (2020) 591–602, <https://doi.org/10.1007/s10237-019-01232-3>. Apr.
- [40] P. Wu, Q. Gao, P. Hsu, On the representation of effective stress for computing hemolysis, *Biomech. Model. Mechanobiol.* 18 (2019) 665–679, <https://doi.org/10.1007/s10237-018-01108-y>.